Cell Reports
Physical Science

CellPress
OPEN ACCESS

Article

Bilayer layer-by-layer structures for enhanced efficiency and stability of organic photovoltaics beyond bulk heterojunctions

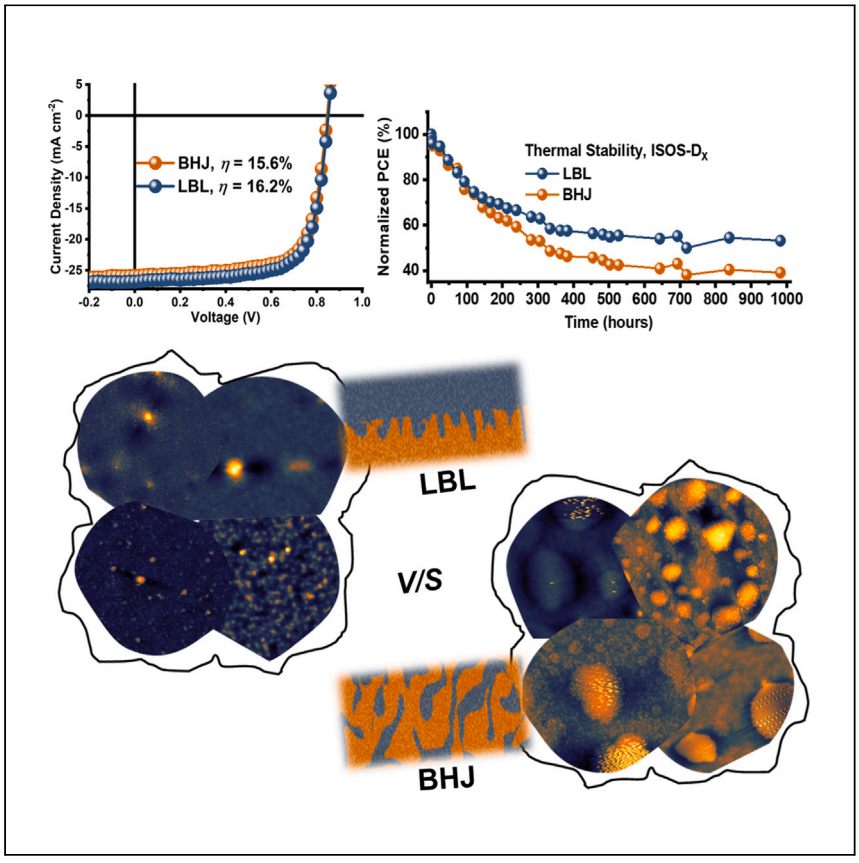

A layer-by-layer organic photovoltaic device with excellent performance is created by tuning individual layers. Kumari et al. report 16.21% efficiency, surpassing the bulk heterojunction equivalent device, and demonstrate improved photostability and thermal stability for nine different non-fullerene acceptor systems.

Tanya Kumari, Irina Vyalih, Miguel Ángel León Luna, ..., Jens Wenzel Andreasen, Vida Turkovic, Morten Madsen

tanyaisara@gmail.com (T.K.)
madsen@mci.sdu.dk (M.M.)

Highlights

Carefully tuning layer-by-layer thicknesses results in high-performance organic photovoltaics

A 16.21% efficiency is achieved, outperforming the bulk heterojunction counterpart

Photo-/thermal stability of layer-by-layer build is demonstrated for 9 distinct systems

Improved stabilities are due to reduction in phase aggregation seen in bulk heterojunctions

Kumari et al., Cell Reports Physical Science 5, 102027
June 19, 2024
https://doi.org/10.1016/j.xcrp.2024.102027

Please cite this article in press as: Kumari et al., Bilayer layer-by-layer structures for enhanced efficiency and stability of organic photovoltaics beyond bulk heterojunctions, Cell Reports Physical Science (2024), https://doi.org/10.1016/j.xcrp.2024.102027

Cell Reports
Physical Science

Article

Bilayer layer-by-layer structures for enhanced efficiency and stability of organic photovoltaics beyond bulk heterojunctions

Tanya Kumari,[1,2,*] Irina Vyalih,[1,2] Miguel Ángel León Luna,[1,2] Hamsa Ahmed,[1,2] Mariam Ahmad,[1,2] Rovshen Atajanov,[1,2] Eswaran Jayaraman,[1,2] Suraj Manikandan,[3] Barbara Paci,[4] Aldo Di Carlo,[4,5] Jens Wenzel Andreasen,[3] Vida Turkovic,[1,2] and Morten Madsen[1,2,6,*]

SUMMARY

Tuning bulk heterojunctions is an important step for improving organic photovoltaic device performance; however, challenges remain in obtaining sufficient device lifetimes using this concept. In this work, we report on high-performance PM6/Y7 layer-by-layer organic photovoltaic devices by carefully tuning the layer-by-layer structure and studying the effects on device performance. We demonstrate that an optimized layer-by-layer organic photovoltaic can effectively improve the photophysical properties of the device, resulting in a conversion efficiency of 16.21%, surpassing the bulk heterojunction counterpart. Notably, the developed layer-by-layer device also outperforms the traditional bulk heterojunction in terms of long-term photostability and thermal stability under continuous illumination and temperature stress (85°C) for approximately 1,000 h, with similar results obtained for eight other non-fullerene acceptor systems. The improved long-term photostability and thermal stability in these layer-by-layer systems is ascribed to a mitigation of the strong phase aggregation seen in the bulk heterojunction films.

INTRODUCTION

Organic photovoltaics (OPVs) have been recognized as a potential large-scale photovoltaic technology on the energy market due to their various advantages of low-cost solution processing, light weight, flexibility, scalability, sustainability, and direct compatibility with several applications.[1–4] Owing to the rapid developments of non-fullerene acceptors (NFAs) in the past few years, continuous improvements in power conversion efficiencies (PCEs) of OPVs over 16% have been widely observed, yielding a current record PCE of 19.3%.[5–14] The significant PCE improvements have resulted in OPVs rapidly approaching large-scale commercialization; however, in addition to competitive PCEs, long-term stability is a key factor for the commercial success of any photovoltaic technology. For organic photovoltaics, stability and operational lifetime still requires substantial improvement.[1,15–17] In OPV devices, non-ideal exciton generation, dissociation, and charge transport still limits the overall device performance. Therefore, careful tuning of the electronic structure of the electron donor and acceptor molecules, as well as of their nanoscale bulk heterojunction morphology, is required to further push the performance of OPVs.[18–21] This includes their device stability, as the balance between efficient exciton dissociation and charge transport in the photoactive layer should be maintained over time in order to sustain long-term high OPV performance.[5,22] In the

[1]Mads Clausen Institute, Center for Advanced Photovoltaics and Thin Film Energy Devices (SDU CAPE), University of Southern Denmark, 6400 Sønderborg, Denmark

[2]SDU Climate Cluster, University of Southern Denmark, 5230 Odense, Denmark

[3]Department of Energy Conversion and Storage, Technical University of Denmark, 2800 Kongens Lyngby, Denmark

[4]Istituto di Struttura della Materia-CNR (ISM-CNR), Area della Ricerca di Roma - Tor Vergata, Via del Fosso del Cavaliere 100, 00133 Rome, Italy

[5]CHOSE (Center for Hybrid and Organic Solar Energy), Department of Electronic Engineering, University of Rome "Tor Vergata," via del Politecnico 1, 00133 Rome, Italy

[6]Lead contact

*Correspondence: tanyaisara@gmail.com (T.K.), madsen@mci.sdu.dk (M.M.)

https://doi.org/10.1016/j.xcrp.2024.102027

Please cite this article in press as: Kumari et al., Bilayer layer-by-layer structures for enhanced efficiency and stability of organic photovoltaics beyond bulk heterojunctions, Cell Reports Physical Science (2024), https://doi.org/10.1016/j.xcrp.2024.102027

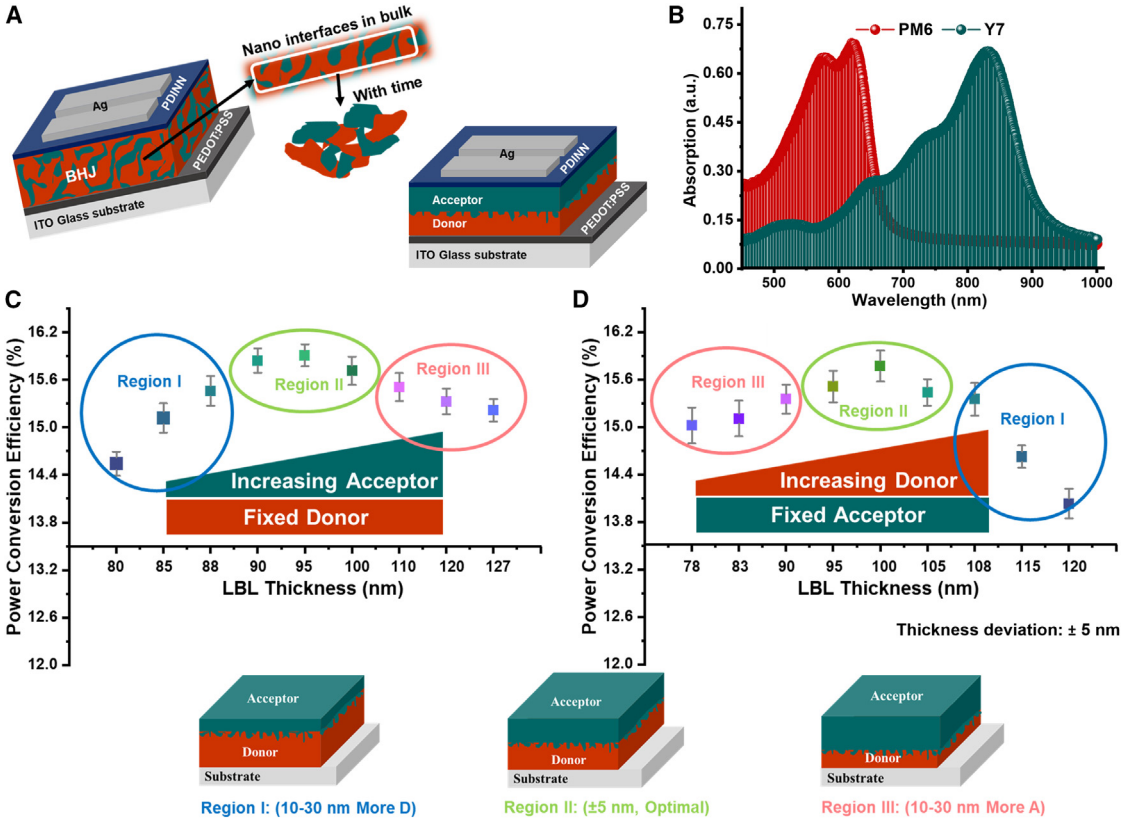

Figure 1. Architectural features, optical characteristics, and initial performance assessment

(A) Device architectures of bulk heterojunction and LBL OPVs.

(B) Absorption spectra of pristine PM6 and Y7 films.

(C and D) Investigation of device performance of PM6- and Y7-based LBL OPVs as a function of (C) acceptor and (D) donor layer thicknesses by varying concentration and rpm. Error bars represent the standard deviation around the mean. Insets are thickness illustrations of regions I (More D), II (Optimal), and III (More A).

past few decades, bulk heterojunction (BHJ) architecture based on organic electron donor and acceptor molecules has gained great success in OPV technology. This architecture gets around the short exciton diffusion length limitation of the donor and acceptor materials by providing an interpenetrating donor/acceptor (D/A) network.[23–26] Nevertheless, an optimized BHJ morphology with abundant D/A interfaces for effective exciton dissociation, and at the same time continuous donor and acceptor domains for efficient charge transport, are necessary throughout the operational period of a highly efficient OPV device.[5,9,27,28] However, the BHJ morphology is only kinetically frozen during solution processing, which is usually far from its thermodynamic equilibrium. Therefore, during prolonged illumination or thermal aging, intrinsic morphological instability is commonly observed in this blend BHJ layer.[29–31] In particular, an evolution of the blend morphology from the kinetically trapped state to the thermodynamically stable state, such as phase aggregation and/or nano D/A interface contraction, will result in severe degradation of charge-transport dynamics and unsatisfactory lifetime of OPVs (Figure 1A).[26,32,33] In this regard, several effective strategies have been thoroughly investigated to considerably lower this degradation effect in BHJ OPVs, using for example solid additives that promote a specific morphology as well as introducing a third component in ternary blending of OPV active layers.[34–38] However, as the BHJ's nanoscale domains gradually approach equilibrium state, they typically demix D/A domains on

Please cite this article in press as: Kumari et al., Bilayer layer-by-layer structures for enhanced efficiency and stability of organic photovoltaics beyond bulk heterojunctions, Cell Reports Physical Science (2024), https://doi.org/10.1016/j.xcrp.2024.102027

a large scale, leading to phase-aggregated morphology.[39] As a result, very few state-of-the-art BHJ OPVs have been able to satisfactorily provide a long lifetime under illumination or thermal aging so far.[21,40–42]

One of the ways to eliminate the necessity to maintain the complex nanoscale D/A network, which compromises the charge transport in these BHJ OPVs over time, is by adopting a layer-by-layer (LBL) architecture fabricated through a sequential processing approach (Figure 1A).[35,36,43–47] Although this LBL, also called bilayer architecture, has been investigated for a long time, the limited diffusion length (L_D) of fullerenes (~10 nm) has prevented the development of efficient LBL OPVs. Owing to the recent development of NFAs with higher L_D values (30–45 nm), enabling efficient exciton diffusion to the D/A interface, the LBL approach has now become a viable and performance-competitive architecture.[48–50] In this LBL processed architecture, donor and acceptor layers are independently controlled without involving the time-consuming optimization procedures to fine-tune the nanoscale morphology. In the LBL architecture, each layer has only one type of organic semiconducting material and, hence, more condensed packing and thermodynamically stable morphology for each layer can be obtained, which contrasts with the intrinsically unstable nanoscale mixed domains in the BHJ architecture.[21,35,36,39,51,52]

In this work, we present a detailed study unveiling the significance of adopting LBL device architectures in the field of OPV technology. A thorough investigation of LBL architecture as a function of donor and acceptor thickness on the performance of PM6-based (also known as PBDB-T-2F) and Y7-based (also known as BTP-4Cl) OPV[9,10,53] have been carried out. The optimized LBL OPV interestingly demonstrated enhanced device performance with PCE of 16.2%, even surpassing that of the BHJ architecture. Here, morphology, charge generation, and transport, as well as recombination dynamics, are systematically studied using several electrical, optical, morphological, and spectroscopic measurements to shed light on these findings. Following Summit on Organic Photovoltaic Stability (ISOS) protocols, the developed LBL OPV is then compared with the conventional BHJ OPV in terms of long-term photostability and thermal stability. Interestingly, the LBL devices show superior long-term photostability and thermal stability as compared to the BHJ architecture.[54] In this study, detailed electrical, optical, and morphological characterization using UV-visible (UV-vis) spectroscopy, Fourier transform infrared (FTIR) spectroscopy, energy-resolved electrical impedance spectroscopy (ER-EIS), optical microscopy, scanning electron microscopy (SEM), and atomic force microscopy (AFM) is utilized to shed light on the degradation phenomena in both LBL and BHJ architecture. Importantly, to demonstrate the robustness of LBL architecture over BHJ, we analyzed eight more highly efficient non-fullerene systems, namely PM6 & Y6, PM6 & N3, PM6 &Y7-12, PM6 & IT-4F, TPD-3F & IT-4F, PBDB-T & ITIC, PTB7-Th & EH-IDTBR, and PTB7-Th & O-IDTBR,[2,6–10,12,21,28,37,53,55–58] to enable a conclusion on the general validity of these findings. Indeed, higher long-term photostability and thermal stability in these systems are generally observed for LBL architectures compared to BHJ architectures. Notably, all BHJ structures in these systems show the presence of large aggregation upon degradation, as evidenced from AFM analysis, which lowers the performance over time, supporting the resilience of LBL architectures in future OPV technology.

RESULTS AND DISCUSSION

Layer-by-layer structure morphology

Although there have been recent reports on non-fullerene OPV LBL devices, detailed studies on the effect of thickness and morphology of each layer, as well

Please cite this article in press as: Kumari et al., Bilayer layer-by-layer structures for enhanced efficiency and stability of organic photovoltaics beyond bulk heterojunctions, Cell Reports Physical Science (2024), https://doi.org/10.1016/j.xcrp.2024.102027

as the interface, for fully solution-processed LBL devices are still missing. We begin this section with a detailed examination of the morphology of our D/A layers. First, we demonstrate that sequential spin-coating of the acceptor layer over the donor layer, to produce LBL devices, does not significantly change the molecular orientation of the donor underlayer. For this part, we employed thickness measurement using AFM, and molecular orientation characterization using grazing incidence wide-angle scattering (GIWAXS) on the donor, donor-washed, and LBL films (Figure S1). For the donor-washed film, pure acceptor solvent is spin-coated on top of the donor layer, similarly as the acceptor layer would be spin-coated on top, but here without the actual acceptor molecules. Importantly, these donor-washed films show a negligible effect on molecular orientation when compared to the untreated donor layer. This indicates that the acceptor layers can be deposited on top of the donor layer without significantly altering the surface topography of the underlying donor film.[59–61] To determine the interface thickness, we measured the energy-dispersive X-ray reflectometry (EDXR) pattern of the PM6/Y7 LBL (Figure S2). The details of the measurement and analysis are provided in the supplemental information. The EDXR profile Parratt fitting accounts for a single layer with a thickness of 945 ($\pm$0.5) Å (the PM6/Y7 interface could not be resolved), which in fact corresponds to adding the nominal thicknesses of the PM6 and Y7 layers in the LBL structure. Additionally, the LBL combined surface (Y7) and buried interface (glass/PM6) roughness is only 3.0 ($\pm$0.5) Å.

Photovoltaic performance

Next, we thoroughly examined the LBL OPV as a function of donor (PM6) and acceptor (Y7) thicknesses, as seen in Figures 1C and 1D (see Figures S3A and S3B for detailed device parameters). To study the OPV performance, we fabricated LBL devices in the configuration of ITO/PEDOT:PSS/PM6/Y7/PDINN/Ag, for which the processing conditions are documented in experimental procedures. In Figure 1C, the donor thickness is first fixed by fixing the concentration and spin-coating speed (rotations per minute [rpm]), and the acceptor concentrations and spin-coating rpms are gradually tuned to increase the overall LBL thickness (Figure S4). In Figure 1D, the donor concentrations and spin-coating rpms are gradually tuned (Figure S5) while keeping the acceptor concentration and spin-coating rpm constant. To simplify our study, we have divided this performance analysis into three regions, as can be seen in the insets of Figures 1C and 1D. Region I (blue color) with roughly 10–30 nm higher thickness of donor (labeled More D), region II (green color) with $\pm$5 nm thickness deviation of each donor or acceptor (labeled Optimal), and region III (light red) with roughly 10–30 nm higher thickness of acceptor (labeled More A), have been studied in detail. However, it should be noted that due to the use of a common solvent for depositing donor and acceptor layers, the interfaces are not sharp and a thin BHJ-like interface is likely to be present between the two layers. The UV-vis near-infrared absorption spectra of More D, Optimal, and More A LBL films are shown in Figure S6. It should be noted that the tuning of donor layer and acceptor layer thicknesses is done in the same batch, and the device performance in Figures 1C, 1D, and S4 (see supplemental information) is presented with emphasis on the thickness-performance correlation of each layer rather than reporting the highest PCE. The More D LBL OPV devices with higher donor thickness demonstrated the lowest performance in both cases (Figures 1C and 1D). The lower exciton diffusion length of PM6 (<15 nm), leading to insufficient dissociation of excitons at the D/A interface, results in lowering of mainly the short-circuit current density (J_{SC}), and fill factor (FF) (Figure S3).[48,49] The devices with a nearly equal thickness of donor and acceptor demonstrate superior performance, also larger than the More An LBL devices having higher acceptor thickness. The improved device parameters

Please cite this article in press as: Kumari et al., Bilayer layer-by-layer structures for enhanced efficiency and stability of organic photovoltaics beyond bulk heterojunctions, Cell Reports Physical Science (2024), https://doi.org/10.1016/j.xcrp.2024.102027

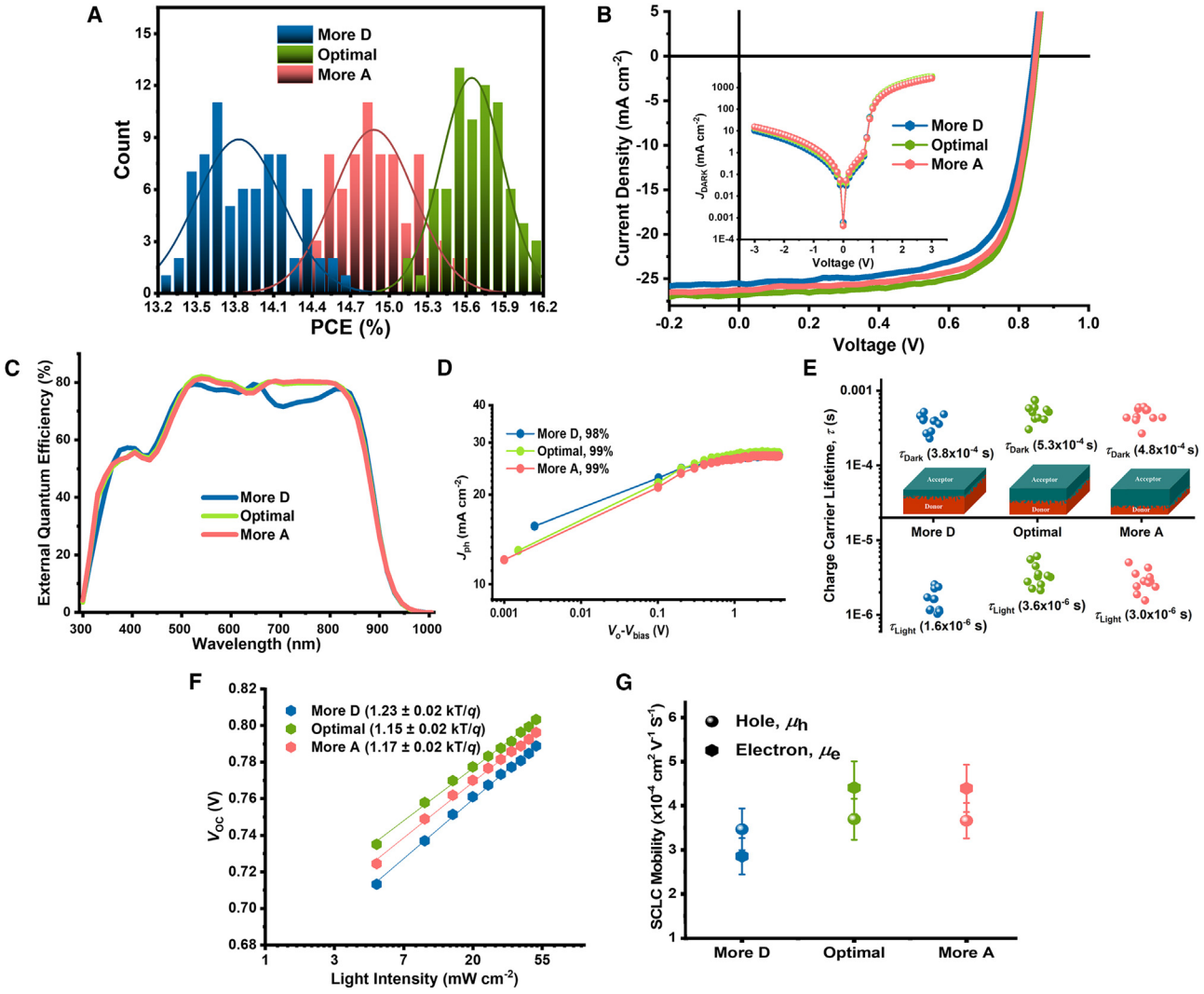

Figure 2. Device performance, charge transport, and recombination dynamics of LBL OPVs

(A) Histograms of the PCE counts.

(B) *J-V* characteristics under AM 1.5G irradiation at 100 mW cm^{-2} (inset: *J-V* characteristics in darkness).

(C) EQE curves.

(D) J_{ph} versus V_{eff} characteristics.

(E) Charge-carrier lifetimes (τ) using transient photovoltage curves.

(F) Dependence of open-circuit voltage (V_{OC}) on light intensity.

(G) Electron (μ_e) and hole (μ_h) mobilities for More D-, Optimal-, and More A-based LBL devices; error bars represent the standard deviation around the mean. SCLC, space-charge-limited curve.

in the Optimal case indicates improved charge generation, dissociation, and transport dynamics in these devices, which are studied in the following section. Further fine-tuning of thicknesses in Optimal LBL OPV is also conducted, as seen in Figure S7.

Figure 2A displays the PCE distribution histogram for 75 independently measured devices of More D, Optimal, and More A, indicating good reproducibility of device performance in the three cases. The current density-voltage (*J-V*) characteristics and the corresponding external quantum efficiency (EQE) curves for the best-performing devices under AM 1.5G irradiation (100 mW cm^{-2}) are shown in Figures 2B and 2C,

Please cite this article in press as: Kumari et al., Bilayer layer-by-layer structures for enhanced efficiency and stability of organic photovoltaics beyond bulk heterojunctions, Cell Reports Physical Science (2024), https://doi.org/10.1016/j.xcrp.2024.102027

Table 1. Performance analysis of LBL architecture

	V_{OC} (V)	J_{SC} (mA/cm^{-2})	Fill factor (%)	PCE (%) (max)	$J_{integ.}$ (mA/cm^{-2})	R_s (Ω)	R_{sh} (Ω)
More D	0.843 ± 0.003	25.08 ± 0.62	67.3 ± 1.5	13.98 ± 0.65 (14.63)	24.30	20.84 ± 8.63	(1.05 ± 0.24) E+04
Optimal	0.846 ± 0.003	26.15 ± 0.66	71.6 ± 1.4	15.67 ± 0.54 (16.21)	24.90	14.54 ± 6.11	(1.22 ± 0.25) E+04
More A	0.844 ± 0.003	26.04 ± 0.60	69.2 ± 1.4	15.02 ± 0.61 (15.62)	24.76	17.42 ± 7.02	(1.12 ± 0.23) E+04

Device parameters of optimized More D-, Optimal-, and More A-based LBL devices under AM 1.5G irradiation at 100 mW cm^{-2} Average of 50 devices in each case. Data in parentheses correspond to maximum value.

respectively. As seen in the photovoltaic parameters listed in Table 1, the devices with higher donor thickness (More D) showed the lowest V_{OC}, J_{SC}, and FF, resulting in minimal PCE of 14.63% (13.98 ± 0.65) compared to the other two cases. The Optimal LBL devices with nearly equal thickness of donor and acceptor achieved a maximum PCE of 16.21%, with V_{OC} of 0.846 ± 0.003 V, J_{SC} of 26.15 ± 0.66 mA cm^{-2}, and FF of 71.6 ± 1.4, while devices with higher acceptor thicknesses (More A) demonstrated maximum PCE of 15.62% with nearly similar device parameters as Optimal. The I_{on}/I_{off} ratio (Table S1) obtained from dark *J-V* characteristics of the inset in Figure 2B shows the highest rectification ratio for Optimal LBL devices, indicating the occurrence of effective charge extraction, which is also responsible for the observed higher FF of ~73%, compared to the other two cases.

Charge-transport and recombination dynamics

To understand exciton dissociation, charge transport, and recombination dynamics in the LBL devices with different thicknesses of donor and acceptor layers, we carried out a series of electrical characterizations of the devices.[62–65] First, we measured the photocurrent density (J_{ph}) of the devices as a function of the effective voltage (V_{eff}), as shown in Figure 2C (see electrical characterization in the experimental procedures for additional details). Under this short-circuit condition, the LBL OPV devices with higher donor thickness showed the lowest exciton dissociation probability (P_{diss} = $J_{ph,sc}/J_{ph,sat}$) compared to the other devices, as shown in Table S1. This confirms that the limited diffusion length of PM6 donor can limit the LBL OPV performance at higher thicknesses. Charge-carrier lifetimes in LBL devices were determined using transient photovoltage (TPV) as a function of illumination intensities ranging from 0.0 to 0.5 sun (Figures S8A–S8D). These lifetimes in the devices are typically associated with the charge carrier's steady-state recombination rate.[66–70] As shown in Figure 2D, it is observed that the average charge-carrier lifetimes, τ (s), are lowest for LBL devices with higher donor thicknesses, and interestingly the $\tau_{avg.}$ (s) for Optimal is larger than that for LBL OPV with higher acceptor thicknesses (More A). This indicates that the balanced thickness of both donor and acceptor is necessary for efficient charge transport. We then measured the light-intensity dependence of the *J-V* characteristics to understand the recombination kinetics of the devices (Figures 2D and S9). In general, the relationship between the J_{SC} values and the incident light intensity (P_{light}) values adhered to a power-law dependence, $J_{SC} \propto P^{\alpha}_{light}$, whereas the V_{OC} values showed a natural logarithm dependence of P_{light}, with a slope of nkT/q, where k is Boltzmann's constant, T is temperature, q is elementary charge, and n is the ideality factor. As shown in Figure 2D, n = 1.15 ± 0.02 suggests that geminate or trap-assisted Shockley-Read-Hall recombination responsible for the loss of free-charge carriers is lowest in the Optimal LBL devices.[62,64] The weakest bimolecular recombination with $\alpha \sim 0.99$ in the Optimal case, whereas the lower $\alpha \sim 0.95$ and $\alpha \sim 0.99$ in More D and More A LBLs, respectively, also confirms the improved charge transport in the devices with equal thickness of donor and acceptor. To obtain additional insight into the observed performance trend by tuning the D/A thicknesses, the hole and electron mobilities of the blend films were

Please cite this article in press as: Kumari et al., Bilayer layer-by-layer structures for enhanced efficiency and stability of organic photovoltaics beyond bulk heterojunctions, Cell Reports Physical Science (2024), https://doi.org/10.1016/j.xcrp.2024.102027

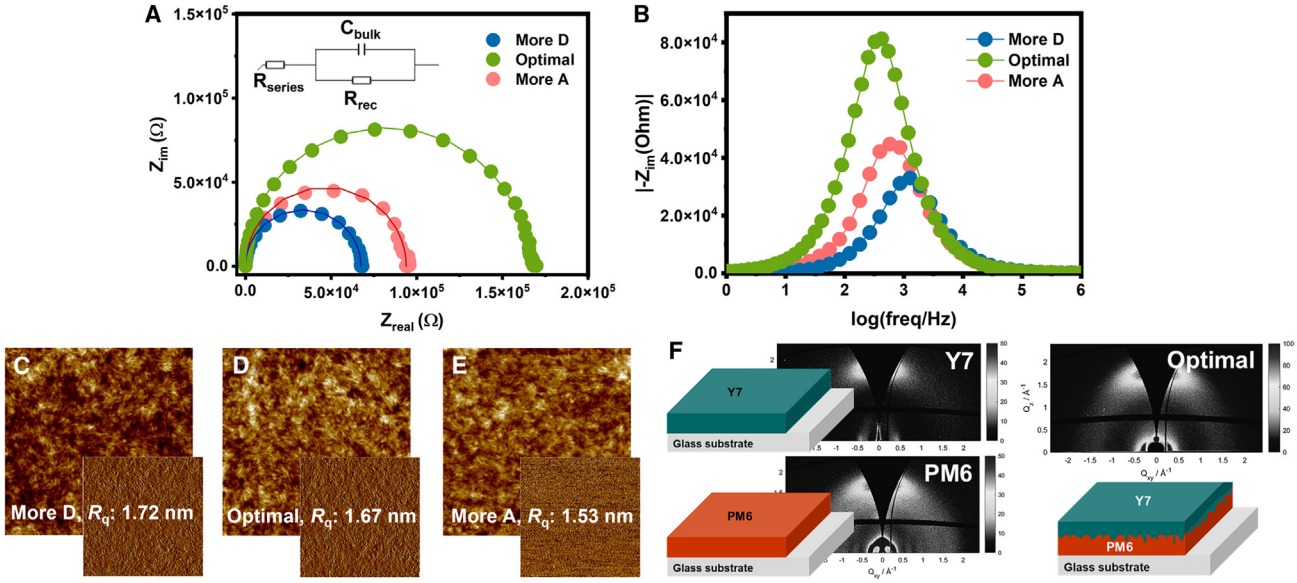

Figure 3. Electrical and morphological characteristics of LBL OPVs

(A) Nyquist plots (inset: equivalent circuit employed in fitting different impedance curves).

(B) Frequency-dependent imaginary parts of the impedance spectra.

(C–E) AFM topography height and phase images (scan size 2 × 2 μm) of (C) More D-, (D) Optimal-, and (E) More A-based LBL films.

(F) GIWAXS images of PM6, Y7, and Optimal LBL films.

determined by fitting the dark current to the model of a single-carrier space-charge-limited curve (Figures 2G and S10), as described by the Mott-Gurney equation.[28,36,64,71,72] More balanced hole (μ_h)/electron (μ_e) mobilities of 4.41 × 10^{-4}/3.70 × 10^{-4} cm^2 V^{-1} s^{-1} and 4.40 × 10^{-4}/3.66 × 10^{-4} cm^2 V^{-1} s^{-1} were obtained for the Optimal and More A-based LBL OPVs as compared to the LBLs with higher donor thickness (More D), 2.85 × 10^{-4}/3.47 × 10^{-4} cm^2 V^{-1} s^{-1}. This observed mobility trend suggests the lowest recombination loss in the Optimal LBL OPV with enhanced J_{SC} and FF values in the devices, as also observed in the preceding section.

To quantify resistive and capacitive contributions to the overall electrical response of the devices with different layer thicknesses, we undertook EIS of the LBL systems.[73–75] Figure 3A shows Nyquist plots of the LBL devices over the frequency range of 10 Hz to 1 MHz. The fitted curves are shown in Figure 3A as lines together with the experimental data (denoted as symbols), where a simplified circuit model was used to fit these curves (inset of Figure 3A). All Nyquist plots showed a single semicircle in the complex plot of the imaginary part versus the real part of the complex impedance. The corresponding parameters are listed in Table S1. In this circuit, R_{series} represents the ohmic series resistance including the electrode and bulk resistance in the active layer. R_{rec} is associated with the charge recombination resistance according to the model employed. We observed that the Optimal LBL OPV showed the highest non-radiative recombination resistance R_{rec} value (≈164.9 kΩ), whereas LBL with higher donor thickness showed the lowest R_{rec} value (≈67.4 kΩ), indicating that the LBL with higher donor thickness suffers from highest charge recombination, even higher than devices with higher acceptor thickness R_{rec} value (≈93.8 kΩ). As can be seen from the frequency-dependent imaginary parts in Figure 3B, the maximum frequency (f_{max}) value in the impedance is located at a lower frequency for the Optimal case compared with that of More A or More D. The f_{max} is related

Please cite this article in press as: Kumari et al., Bilayer layer-by-layer structures for enhanced efficiency and stability of organic photovoltaics beyond bulk heterojunctions, Cell Reports Physical Science (2024), https://doi.org/10.1016/j.xcrp.2024.102027

to the relaxation time (τ) by $f_{max} \propto 1/\tau$; this implies that Optimal LBL devices had higher electron lifetimes and diffusion rates, which is consistent with the charge-carrier lifetime obtained in aforementioned TPV measurement.

Using AFM and GIWAXS, the impact of the processing solvents on the morphology and molecular orientation of the Optimal LBL films was further investigated.[2,6–9,34,72,76] In Figures 3C–3E, the More D, Optimal, and More A films showed similar features in AFM height and phase images, indicating that the layers show similar morphological characteristics. As also seen in GIWAXS images in Figure 3F, the molecular orientations of PM6 and Y7 were essentially preserved in the LBL films. We did not observe any distinct changes upon tuning the thicknesses. From GIWAXS images in Figures S11A and S11B, both PM6 and Y7 have strong, well-defined (010) π-π stacking in the out-of-plane (q_z) direction centered at around 1.70 $Å^{-1}$, and 1.73 $Å^{-1}$, respectively, indicating the thermodynamically preferred face-on orientation of donor and acceptor material. The Optimal LBL OPV has a similar face-on orientation with a strong peak for (010) π-π stacking at around 1.75 $Å^{-1}$ in the q_z direction (Figure S11C). The *d*-spacing and crystallite coherence length for (100) lamellar and (010) π-π stacking in the out-of-plane (q_z) direction obtained from line cut profiles of GIWAXS data for PM6, Y7, and LBL films are provided in Table S2. Figures S12A and S12B display the circular cut profiles of the (010) π-π diffraction peaks and (100) lamellar diffraction peaks. The azimuthal angle (χ) intensity of 45°–135° was attributed to the substrate's parallel (||) π-π stacking, while the χ intensity of 0°–45° and 135°–180° was attributed to the perpendicular ($\perp$) π-π stacking, and vice versa for the lamellar stacking.[74] The nearly identical circular cut profiles of the (100) lamellar and (010) π-π stacking of LBL film compared to pristine PM6 and Y7 indicates that molecular orientation was essentially preserved in the LBL devices.

Architectural robustness with respect to photoannealing and thermal annealing

Besides the requirement of a high PCE, improvement in long-term photostability and thermal stability is of paramount importance to ensure a long lifetime under continuous operation even in harsh conditions.[11,18,30,39,42,54,55,77–79] To gain further insights into the long-term architectural stability, the Optimal LBL OPV, showing superior device and electrical performance, was compared in detail with the BHJ OPV counterpart. PM6:Y7-based BHJ devices with similar 100-nm thickness were fabricated according to the reported literature, as detailed in experimental procedures. The *J-V* characteristic of best-performing PM6:Y7 BHJ OPV is provided in Figure S14. The maximum PCE of 15.6%, with V_{OC} of 0.845 V, J_{SC} of 25.88 mA cm^{-2}, and FF of 71.5%, is achieved for the BHJ OPV, which is interestingly below the maximum performance of the Optimal LBL OPV. To compare the intrinsic stability of the optimized LBL and BHJ devices, we performed a comparative study of the two architectures by subjecting the OPVs to photostress and thermal stress over a relatively long time inside a nitrogen-filled glovebox. The stability test of state-of-the-art OPVs was carried out by following ISOS protocols in inert atmosphere, which largely reveals the inherent stability of the active layers.[54] We used maximum power point (MPP) tracking, and Figure S15A shows the PCE extracted from continuous MPP tracking (black) versus periodic *J-V* scans (red) collected during the measurement. The detailed ISOS protocols are summarized in Table 2. To emphasize structural stability, we used a UV filter (Figure S15B) to prevent the rapid degradation of the active layer in photostability measurement. Second, an important stress factor in maintaining structural stability is temperature. Thermal degradation in the dark occurs in OPVs at elevated temperatures due to chemical and, especially, structural and morphological instabilities of the absorber materials. Three devices for both the

Please cite this article in press as: Kumari et al., Bilayer layer-by-layer structures for enhanced efficiency and stability of organic photovoltaics beyond bulk heterojunctions, Cell Reports Physical Science (2024), https://doi.org/10.1016/j.xcrp.2024.102027

Table 2. ISOS protocol

Stability	Light source	Intensity	Atmosphere	UV filter	Temp. (°C)	Encapsulation	MPP tracking	Interval
Photo (ISOS-L_X)	solar simulator	1 sun	N_2-filled chamber	yes	35–50	no	yes	15 min
Thermal (ISOS-D_X)	solar simulator	1 Sun	N_2-filled chamber	no	85	no	–	–

Summary of ISOS parameters used for the photoannealing and thermal annealing of optimized LBL and BHJ OPVs.

LBL and BHJ OPV cases were studied in photostability and thermal stability tests, and the corresponding PCE, V_{OC}, J_{SC}, and FF are shown in Figures S16–S19, respectively. Figure 4A shows that the photostability (ISOS-L_X) of the LBL OPV demonstrated that 74% of the initial PCE could be maintained after continuous light illumination for ~1,000 h, while the BHJ OPV retained only 67% within the same time period. As shown in Figures S20 and S21, we also measured the photostability without a UV filter, and the initial degradation profile for ~300 h appears very similar to the one measured with a UV filter. While in the photostability measurements a slow performance reduction over time was observed, the thermal annealing measurements of OPV devices (Figure 4B) showed more continuous deterioration in performance. When considering the thermal stability at 85°C (ISOS-D_X), the LBL OPV retained 53% of the initial PCE after being under continuous thermal stress for ~1,000 h, while the BHJ OPV showed severe degradation with retained PCE of just 39% over the same time period.

Molecular and morphological changes in long-term stability

To uncover the origin of the reduction in PCEs in photostability and thermal stability, we carried out a series of optical, morphological, molecular, and electrochemical characterizations.[2,29,39,41,50,80–82] First, we looked at photodegradation using UV-vis absorption spectra of photodegraded LBL and BHJ films (Figure S22). As can be seen in Figures S22A and S22B, the absorption profiles of both BHJ and LBL films are reduced particularly in the PM6 region due to the photochemical instability of the polymers compared to the Y7, and as a result the current decreased over time, leading to the PCE decrease. Using FTIR spectroscopy, the vibrational modes of the molecules were explored, providing valuable insight into the photodegradation of PM6 and Y7 in the bulk and LBL systems.[83,84] As shown in Figure S23, we assigned the vibrational normal mode at 1,648.20 cm^{-1} to the vibrations of oxygen and carbon atoms of the carbonyl (C=O) group of PM6 and that at 2,216.24 cm^{-1} to the vibrations of nitrogen and carbon atoms of the side-chain cyanide (C≡N) group of Y7. A large shift of C=O peak of the PM6 from 1,648.20 cm^{-1} to 1,646.27 cm^{-1} and 1,645.30 cm^{-1}, and a small shift of C≡N peak of the Y7 from 2,215.28 cm^{-1} to 2,214.32 cm^{-1} and 2,214.32 cm^{-1}, were observed for LBL and BHJ films, respectively. This indicated that the PM6 component tends to undergo more photochemical degradation than Y7, which is consistent with the observed absorption spectra. It should be noted that we did not observe any significant change in the peak intensities for architectures of LBL- and BHJ-based OPV, as the molecular components (i.e., PM6 and Y7) of both architectures are essentially the same. Next, we used optical microscopy (OM) (Figure S24), AFM (Figure S25), and SEM (Figure S26) imaging to analyze the morphological stability. As seen in Figures 4C and 4E, the LBL films showed robustness in the photoannealed films when compared with the fresh ones, whereas the appearance of a fine dotted structure in OM and higher roughness in AFM images was observed for photodegraded BHJ films (Figures 4D and 4F). This can partly explain the lower PCE stability in the corresponding BHJ devices when compared to the LBL devices. Here we suggest that the observed morphological instability in the BHJ devices is more due to the absorbed

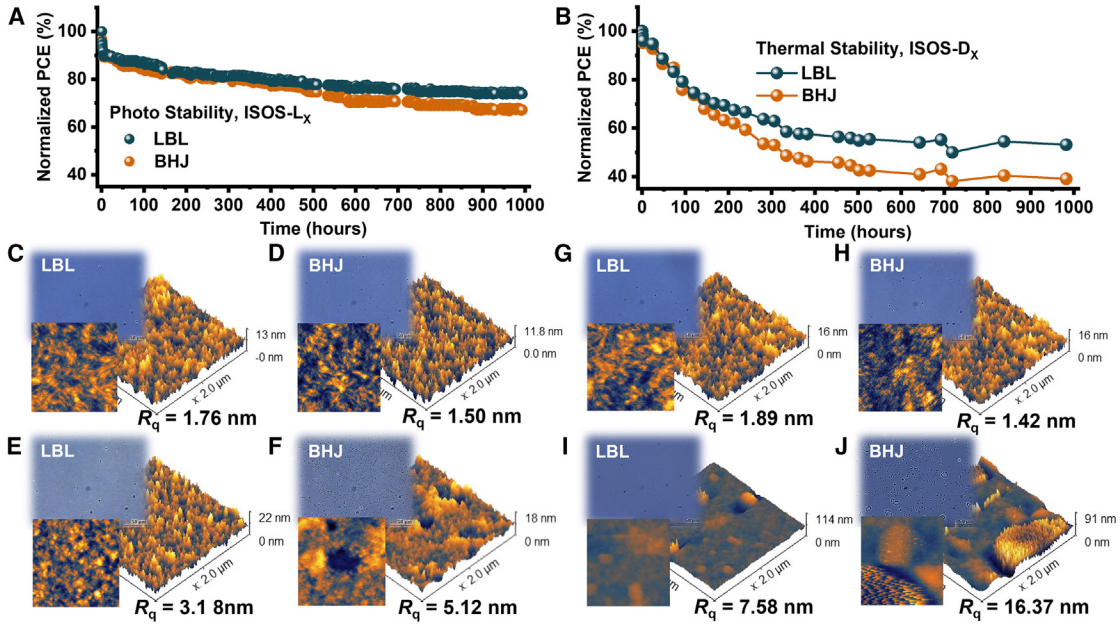

Figure 4. Long-term stability using ISOS protocols and morphological comparison of LBL and BHJ OPVs

(A) Photostability (ISOS-L$_X$).

(B) Thermal stability (85°C, ISOS-D$_X$) comparison of PM6- and Y7-based LBL and BHJ OPVs for 1,000 h under AM 1.5G irradiation at 100 mW cm^{-2}.

(C–J) Corresponding OM and AFM images of fresh (C and G) LBL films and (D and H) BHJ films. Morphological comparison using photodegraded (E) LBL and (F) BHJ films and thermally degraded (I) LBL and (J) BHJ films.

heat during the photostability experiment, which can be understood more clearly in the following morphological characterization of thermally degraded films.[29,39,80]

Next, we compared the optical changes using UV-vis absorption spectra of LBL and BHJ films (Figure S27) for the thermal stability case. In thermally degraded films, a negligible reduction in absorption profile was observed for LBL and BHJ architectures compared to the photostability case. This implied that the thermal stress causes structural instability rather than chemical instability, as expected and as also evident from the OM (Figure S28), AFM (Figure S29), and SEM (Figure S30) images. As seen in Figures 4E, 4F, 4I, and 4J, the LBL films showed much better robustness under thermal stress compared to the BHJ films. The severe PCE degradation of BHJ OPV during the thermal stress is due to the induced micro-sized features (Figure 4J) rather than nano-sized features (Figure 4I) in the LBL devices arising from thermal stress. As a result, we believe that the micro-sized phase aggregation, leading to large-scale demixing of D/A domains, mainly contributed to the observed large PCE loss in BHJ OPVs and that this to a large extent can be mitigated via the LBL architecture.

Energetics of LBL and BHJ structures under photochemical and thermal stress

Additionally, we investigated the defects arising from photochemical and thermal stress in the LBL and BHJ OPVs using the ER-EIS technique, as detailed in experimental procedures.[60,72,85–87] The density of states (DOS) is inversely proportional to the charge-transfer resistance (R_{ct}) at an applied voltage U according to the following equation:

$$g(E_F = eU) = 1 / ek_{et}\lfloor C \rfloor SR_{ct}, \quad \text{(Equation 1)}$$

where e is the elementary charge, E_F is Fermi energy, k_{et} is the charge-transfer constant, C is the concentration of supporting electrolyte in the interface region of the solid/liquid contact interface, and S is the sample area.

Please cite this article in press as: Kumari et al., Bilayer layer-by-layer structures for enhanced efficiency and stability of organic photovoltaics beyond bulk heterojunctions, Cell Reports Physical Science (2024), https://doi.org/10.1016/j.xcrp.2024.102027

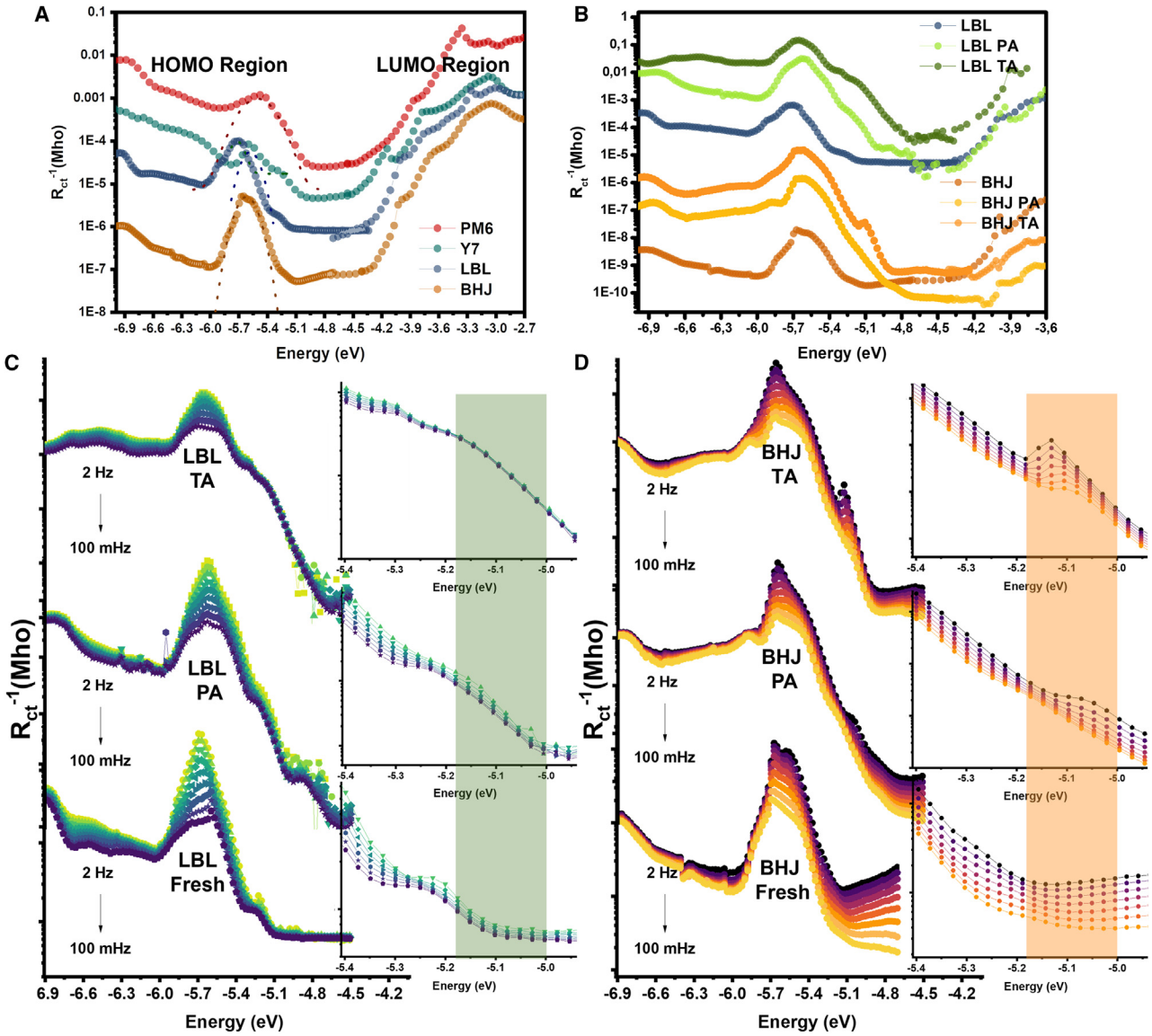

Figure 5. Insight into molecular and device architectural stability of LBL and BHJ OPVs

(A) ER-EIS spectra for fresh PM6, Y7, LBL, and BHJ films at 500 mHz.

(B) Comparison of ER-EIS profiles for photoannealed and thermally annealed PM6- and Y7-based LBL and BHJ films at 500 mHz.

(C) R_{ct}^{-1}-versus-energy plots obtained at fixed frequencies from 100 mHz to 2Hz for fresh, photoannealed (PA), and thermally annealed (TA) (C) LBL and (D) BHJ films. Insets are zoomed images for defective densities of state near HOMO regions.

R_{ct}^{-1}-versus-energy plots were created (Figure 5A) to obtain information about the DOS profiles for PM6, Y7, LBL, and BHJ films, based on Equation 1. The DOS profiles of fresh, photoannealed, and thermally annealed LBL and BHJ films are presented in Figure 5B. The onset of peaks on the left side and right side, as shown in Figure 5A, can be used to electrically determine the highest occupied molecular orbital (HOMO) and lowest unoccupied molecular orbital energy levels, and thus to calculate the electrical band gap of PM6, Y7, LBL, and BHJ films. Figures 5C and 5D show the R_{ct}^{-1}-versus-energy plots obtained at fixed frequencies from 100 mHz to 2 Hz for fresh, photoannealed, and thermally annealed LBL and BHJ films, respectively. Interestingly, on comparing the DOS profiles of LBL and BHJ films in the photoannealing and thermal annealing conditions, the presence of very sharp peaks are observed

Please cite this article in press as: Kumari et al., Bilayer layer-by-layer structures for enhanced efficiency and stability of organic photovoltaics beyond bulk heterojunctions, Cell Reports Physical Science (2024), https://doi.org/10.1016/j.xcrp.2024.102027

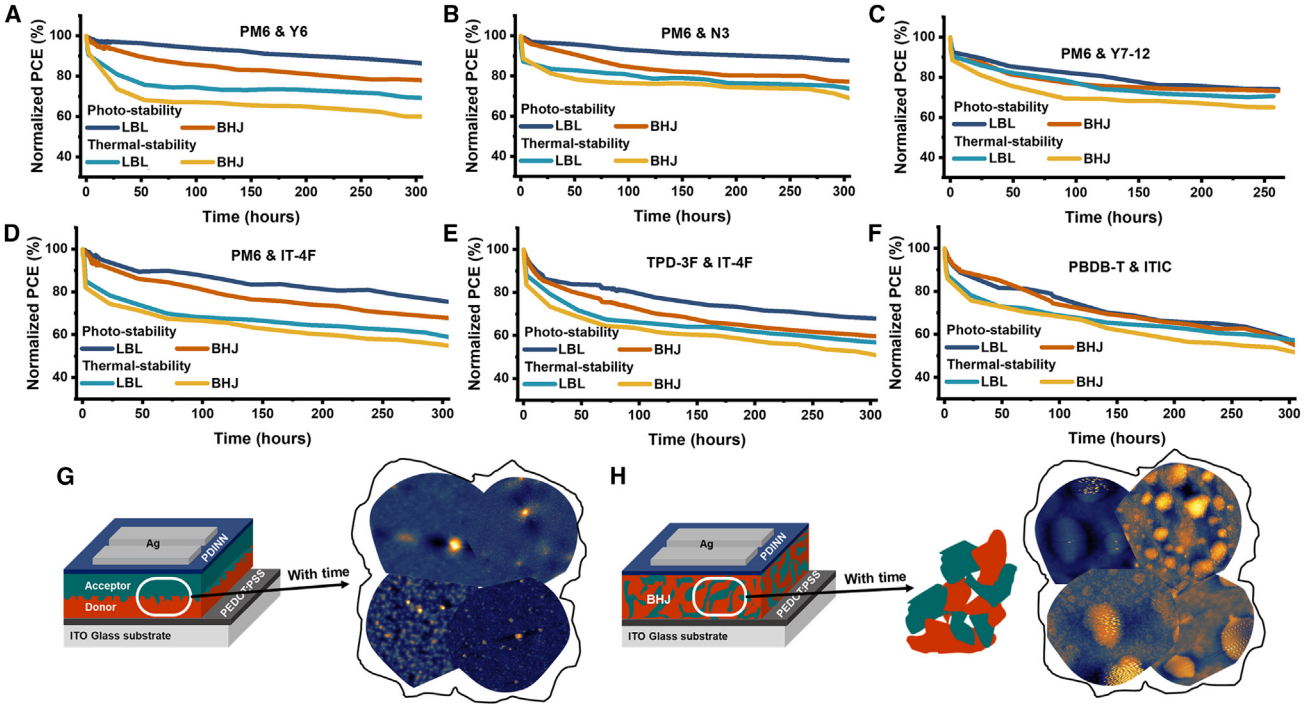

Figure 6. Robustness of LBL architectures over BHJs in different high-performance non-fullerene systems

(A–F) Photostability and thermal stability (85°C) of (A) PM6 & Y6-, (B) PM6 & N3-, (C) PM6 & Y7-12-, (D) PM6 & IT-4F-, (E) TPD-3F & IT-4F-, and (F) PBDB-T & ITIC-based LBL and BHJ OPVs under AM 1.5G irradiation at 100 mW cm^{-2}.

(G and H) Comparison of phase aggregation in (G) LBL and (H) BHJ architectures; based on morphological changes (Figures S31 and S32) after stability measurement.

near the HOMO region (−5.0 to −5.18 eV) for the thermally annealed BHJ films (Figure 5D). This verifies that while the BHJ morphology is kinetically frozen solely during solution processing, this morphology is far from its thermodynamic equilibrium and, therefore, prolonged thermal aging causes the photoactive layer to move toward the thermodynamically stable phase-aggregated state, ultimately modifying the energetics near the HOMO edge and resulting in the unsatisfactory stability performance of the BHJ OPVs. Notably, we observed negligible changes in the DOS profiles of the photoannealed and thermally annealed LBLs compared to the fresh one (Figure 5C), suggesting that the LBL architecture is thermodynamically more stable, as also evident from the device lifetime results.

To further support our findings, we investigated LBL and BHJ OPVs in eight more highly efficient non-fullerene systems, namely, PM6 & Y6, PM6 & N3, PM6 &Y7-12, PM6 & IT-4F, TPD-3F & IT-4F, PBDB-T & ITIC, PTB7-Th & EH-IDTBR, and PTB7-Th & O-IDTBR.[2,6–10,12,21,28,37,53,55–58,82,88–90] Table S3 shows the device parameters of optimized devices, and device fabrication conditions are reported in supplemental experimental procedures. The photostability and thermal stability of LBL and BHJ devices in these systems are provided in Figures 6A–6F and S31. Interestingly, we found that all the LBL OPV showed improved photostability and thermal stability as compared to their BHJ counterparts, due to the better intrinsic stability of the architecture under photochemical and thermal stress. In Figures S32 and S33, we used the AFM technique to understand the morphological evolution in the degraded LBL and BHJ systems upon comparing fresh and degraded films. As shown in the AFM results, we observe that the LBL systems are more robust than the BHJ systems, where the presence of large aggregation can be very clearly

seen in the degraded films. As observed above in detailed characterizations of PM6 & Y7 systems, we also believe here that the presence of nanoscale domains in the optimized morphology of BHJs has gradually and eventually evolved to the thermodynamically stable state, which is quite different from the initial state, showing large-scale phase-aggregated suboptimal morphology that results in the pronounced reduction in PCE with time. Therefore, improved morphology retainment of LBLs (Figure 5G), as compared to BHJs (Figure 5H) in different NFA systems highlights the need in the future to move beyond the BHJ toward the robust LBL architecture in the OPV field. To demonstrate the potential for upscaling using this LBL approach for OPV technology, we have also fabricated LBL films using slot die (S2S) coating to scale up the PM6/Y7 LBL OPV (Figure S34A). A well-defined LBL film can be coated on a large substrate (7 × 7 cm^2), as shown in Figures S34B and S34C. The AFM images of PM6, Y7, and LBL films shown in Figures S34D–S34F are also reflective of the spin-coated results presented in this study, indicating the smooth transfer of the fabrication process from lab scale to large scale.

In this work, OPV LBL architecture devices based on PM6/Y7 were thoroughly examined by varying the donor and acceptor thicknesses and studying in depth the effect on electrical, optical, and morphological properties. It was found that LBL devices with higher donor thicknesses showed the poorest device performance due to inadequate exciton separation and charge generation-extraction, as well as enhanced bimolecular and trap-assisted recombination. The higher-acceptor-thickness LBL devices showed improved electrical properties, but these were still lower than those of the LBL OPV devices with equal donor and acceptor thicknesses, which showed superior charge-transport dynamics with the lowest recombination rate and highest PCE of 16.21%. This even exceeded the PCE of its BHJ counterpart. To investigate the robustness of the LBL architecture, we compared the long-term photostability and thermal stability of the high-performance LBL OPV with conventional BHJ OPV devices by following ISOS degradation protocols. The LBL devices clearly outperformed the BHJ architecture in terms of long-term photostability and thermal stability, with the BHJ devices' poorer performance being attributed to substantial phase aggregation in the film morphology. Notably, ER-EIS showed a significant appearance of DOSs near the HOMO edge region of thermally degraded BHJ films, indicating that the BHJ blend has an intrinsically unstable blend morphology that eventually moves to a thermodynamically stable state, causing severe phase aggregation and performance degradation in the device. To further support our findings and demonstrate their general validity, we also compared the photostability and thermal stability of eight other non-fullerene systems, namely PM6 & Y6, PM6 & N3, PM6 & Y7-12, PM6 & IT-4F, TPD-3F & IT-4F, PBDB-T & ITIC, PTB7-Th & EH-IDTBR, and PTB7-Th & O-IDTBR-based LBL, with BHJ OPV. Compared to BHJ, where severe phase aggregation is clearly seen in films, LBL-architecture-based OPV with nearly frozen film morphology demonstrated enhanced long-term photostability and thermal stability in all cases. Finally, the scaling up of an LBL film using S2S coating techniques was demonstrated to highlight the feasibility of lab-to-fab OPV fabrication. This research thus sheds light on how well performing and robust the optimized OPV LBL architecture is when compared to the widely used BHJ architecture and paves the way for the development of long-term stable LBL OPVs required for commercialization.

EXPERIMENTAL PROCEDURES

Resource availability

Lead contact

Requests for further information and resources should be directed to and will be fulfilled by the lead contact, Prof. Morten Madsen (madsen@mci.sdu.dk).

Materials availability

This study did not generate new unique reagents.

Data and code availability

The primary data supporting the findings of this investigation are included in the article and its supplemental information. The additional datasets produced and/or analyzed during the current investigation can be provided by the corresponding authors upon reasonable request. Additional information is available from the lead contact upon request.

Materials

The donor polymers PM6, TPD-3F, and PTB7-Th, the acceptor materials EH-IDTBR and O-IDTBR, and the electron-transport layer material PDINN were purchased from 1-Material. The donor polymer PBDB-T and the acceptor materials Y7, Y6, Y7-12, N3, ITIC, and ITIC-4F were purchased from Brilliant Matters. To ensure a fair comparison between the experimental and control devices, all active materials employed in this investigation were acquired from the same batch. Poly(3,4-ethylenedioxythiophene) polystyrene sulfonate, (PEDOT:PSS [P VP.AI 4083]) dispersion was purchased from Heraeus. Anhydrous chlorobenzene, anhydrous chloroform, anhydrous methanol, 1-chloronaphthalene (CN), and 1,8-diiodooctane (DIO) were obtained from Sigma-Aldrich and used as received. The additional solvents were provided by TCI and were all used without further purification.

OPV device fabrication and characterization

The pre-patterned indium tin oxide (ITO) glass substrates were cleaned by subsequent 15-min sonication in liquid detergent, deionized water, acetone, and isopropanol, respectively, then dried under nitrogen flow. The substrates were ozone treated before coating the PEDOT:PSS layer. After being spin-coated at 4,000 rpm for 40 s, the PEDOT:PSS layer was annealed for 20 min at 140°C in air. The substrates were subsequently transferred to the glovebox, and the active layer was spin-coated for LBL and BHJ-based OPV device fabrication. The LBL films of donor and acceptor were spin-coated sequentially at different rpms to obtain the desired thicknesses (Figures S5 and S6). The films were then thermally annealed for 10 min at 100°C. Following cooling, a thin PDINN film as an electron-transport layer was spin-coated at 3,000 rpm for 30 s, after which a 100-nm-thick coating of silver was evaporated at 1×10^{-7} bar.

For fabrication of PM6 & Y7 LBL devices, 14 mg mL^{-1} each of the PM6 and acceptor Y7 materials were dissolved in anhydrous chlorobenzene separately and stirred for at least 4 h at 80°C. Prior to spin-coating, 0.5 vol % of CN was added to the solutions. The same recipe was followed for PM6 & Y7-12-based LBL device fabrication. For PM6 & IT-4F, TPD-3F & IT-4F, and PBDB-T & ITIC, the same concentration of donor and acceptor was used, but in the case of PM6 & IT-4F, TPD-3F & IT-4F, and PBDB-T & ITIC 1.0 vol %, 0.5 vol %, and 0.5 vol % of DIO were used, respectively. PM6 & IT-4F solutions were stirred at 40°C, while TPD-3F & IT-4F and PBDB-T & ITIC solutions were stirred at 60°C, for at least 4 h. For PTB7-Th & EH-IDTBR-based and PTB7-Th & O-IDTBR-based LBL device fabrication, 12 mg mL^{-1} each of the PTB7-Th and acceptor materials were dissolved in anhydrous chlorobenzene with 0.5 vol % CN separately, and the solutions were stirred at 60°C for at least 4 h. For PM6 & Y6 and PM6 & N3, 10 mg mL^{-1} each of the PM6 and acceptor materials were dissolved in anhydrous chloroform separately with 0.5 vol % of CN, and the solutions were stirred at 40°C for at least 3 h. The electron-transport layer solution was prepared by stirring 1.0 mg $mL^{-1}$of PDINN in anhydrous methanol at 40°C for 1 h. For BHJ OPV device fabrication, the recipes were followed according to the reported

literature, and approximately similar thicknesses as LBL counterparts (~100 nm) were used.[10,12,36,53,55,56,82,88–90]

After device fabrication, the *J-V* measurements for the photovoltaic devices were carried out using a Keithley 2365 A source measurement unit under Enlitech solar simulator's simulated sunlight (AM 1.5G) at an intensity of 100 mW cm^{-2}. *J-V* curves were measured in the forward direction from −0.5 to 1.2 V, with a dwell time of 5 ms and a scan step of 20 mV. Irradiance was calibrated using a typical silicon photodiode before the device was measured. Four devices were fabricated on one square substrate (1.5 × 1.5 cm^2), and the effective area of each device was 0.066 cm^2, determined by a non-refractive shadow mask. For the photo and thermal stability of LBL and BHJ architectures, the devices were fabricated on smaller substrates (1.0 × 1.5 cm^2, three devices with an active area of 0.028 cm^2) so that the two cases (LBL and BHJ) could be tested simultaneously with the designed setup, allowing for a fair comparison under the same measurement conditions. EQE measurements were carried out utilizing QEX7 quantum efficiency measurement equipment (PV Measurements) in an ambient environment without encapsulating the OPV devices.

Electrical characterizations

For electrical characterizations, OPV devices or active-layer films coated on ITO substrates were used. In exciton dissociation probability, the photocurrent density (J_{ph}) of the devices as a function of the effective voltage (V_{eff}) was measured. J_{ph} is defined as $J_L - J_D$, where J_L and J_D are the current densities under 100 mW cm^{-2} illumination and in dark conditions, respectively. V_{eff} is obtained from the formula $V_{eff} = V_0 - V_{bias}$, where V_0 is the voltage when $J_{ph} = 0$ and V_{bias} is the applied voltage. In the $J_{ph} - V_{eff}$ plot, J_{ph} becomes saturated at a high applied voltage ($V_{eff} \geq 2.0$ V) and this is denoted as $J_{ph,sat}$, which represents the complete dissociation of the photogenerated charges at a high applied voltage. The photocurrent density obtained under the short-circuit condition is referred to as $J_{ph,sc}$. See supplemental information for additional electrical characterization details.

Morphological characterizations

For morphological characterization, the optimized device fabrication processing conditions were used to prepare thin films. Glass substrates were used to fabricate samples for the absorption, OM, SEM, AFM, and thickness measurement, while for all other characterizations, samples were fabricated on silicon substrates. UV-vis spectra were obtained using a UV-1800 spectrophotometer (Shimadzu). OM images were taken with an inverted optical microscope (Olympus, IX71). SEM characterization of the samples was made with a Hitachi Model S-4800 field-emission scanning electron microscope. The images were obtained at an accelerating voltage of 1 kV at 10 μA at working distance of 8 mm. Magnification between 400 nm and 30 μm was used in mixed backscatter and backscattered-electron mode for imaging. The AFM topology measurements of the samples were made with Dimension 3100 AFM equipment and NanoScope Version 5 software. Analysis of the image files was made using Gwyddion software. The scan size of the images is 5 × 5 μm, scan rate 0.40 Hz, and resolution 512 samples per line. Measurements were made in tapping mode. GIWAXS characterization was carried out at the Denmark Technical University using a laboratory setup (Xeuss 3.0, from Xenocs). Here, Cu-Kα radiation (wavelength [λ] = 1.5418 Å) that was supplied by a microfocus copper source was focused and monochromatized with a 2D single-reflection multilayer optic and collimated with scatterless slits. The substrate surface was oriented at a grazing incidence angle of 0.18° with respect to the incident X-ray beam. The scattered radiation was detected with an Eiger 4M single-photon counting detector (DECTRIS),

90.0 mm away from the sample. The raw data were processed and analyzed using MATLAB software.

SUPPLEMENTAL INFORMATION

Supplemental information can be found online at https://doi.org/10.1016/j.xcrp.2024.102027.

ACKNOWLEDGMENTS

M.M. acknowledges financial support from the Independent Research Fund Denmark, Technology and Production Sciences (DFF FTP), for the project ReactPV (grant number 8022-00389B). J.W.A. and M.M. acknowledge financial support from DFF FTP for the project EPIC-OPV, grant no. 1032-00326B. V.T. acknowledges Carlsbergfondet for financial support for the project Artplast (CF20-0531) and Independent Research Fund Denmark for the project Artplast (0217-00245B). This project has received funding from the European Union's Horizon 2020 research and innovation program grant agreement no. 101007084 (CITYSOLAR).

AUTHOR CONTRIBUTIONS

M.M. and T.K. conceived the idea and designed all experimental investigations. T.K. fabricated devices, conducted device characterizations, carried out stability tests, and prepared the films for characterizations. I.V. carried out AFM roughness and SEM measurements. M.A.L.L. carried out EIS and ER-EIS characterizations and assisted in FTIR measurement. R.A. helped with the execution of additional experiments on thermal and photo stability. M.A.L.L. and R.A., supervised by V.T., assisted T.K. in analyzing the relevant experimental results. H.A. carried out AFM thickness measurements. M.A. carried out additional AFM roughness measurements for the roughness and thickness determination of the LBL interfaces. E.J. carried out the scale-up work using S2S technique. J.W.A. and S.M. performed the GIWAXS experiment, and its data analysis was supervised by J.W.A. B.P. and A.D.C. carried out EDXR measurement and analyzed the result. T.K. oversaw the project and contributed to all phases of analysis and experimental design. The manuscript was written by T.K. and M.M. with input from all authors.

DECLARATION OF INTERESTS

There are no conflicts to declare.

Received: October 18, 2023
Revised: December 22, 2023
Accepted: May 14, 2024
Published: June 6, 2024

REFERENCES

1. Riede, M., Spoltore, D., and Leo, K. (2021). Organic Solar Cells—The Path to Commercial Success. Adv. Energy Mater. *11*, 2002653. https://doi.org/10.1002/aenm.202002653.

2. Yan, C., Barlow, S., Wang, Z., Yan, H., Jen, A.K.Y., Marder, S.R., and Zhan, X. (2018). Non-fullerene acceptors for organic solar cells. Nat. Rev. Mater. *3*, 18003. https://doi.org/10.1038/natrevmats.2018.3.

3. Zhang, G., Zhao, J., Chow, P.C.Y., Jiang, K., Zhang, J., Zhu, Z., Zhang, J., Huang, F., and Yan, H. (2018). Nonfullerene Acceptor Molecules for Bulk Heterojunction Organic Solar Cells. Chem. Rev. *118*, 3447–3507. https://doi.org/10.1021/acs.chemrev.7b00535.

4. Zhang, J., Tan, H.S., Guo, X., Facchetti, A., and Yan, H. (2018). Material insights and challenges for non-fullerene organic solar cells based on small molecular acceptors. Nat. Energy *3*, 720–731. https://doi.org/10.1038/s41560-018-0181-5.

5. Zhu, L., Zhang, M., Xu, J., Li, C., Yan, J., Zhou, G., Zhong, W., Hao, T., Song, J., Xue, X., et al. (2022). Single-junction organic solar cells with over 19% efficiency enabled by a refined double-fibril network morphology. Nat. Mater. *21*, 656–663. https://doi.org/10.1038/s41563-022-01244-y.

6. Pan, M.-A., Lau, T.-K., Tang, Y., Wu, Y.-C., Liu, T., Li, K., Chen, M.-C., Lu, X., Ma, W., and Zhan, C. (2019). 16.7%-efficiency ternary blended organic photovoltaic cells with PCBM as the acceptor additive to increase the open-circuit voltage and phase purity. J. Mater. Chem. A *7*, 20713–20722. https://doi.org/10.1039/C9TA06929A.

7. Lin, Y., Firdaus, Y., Nugraha, M.I., Liu, F., Karuthedath, S., Emwas, A.-H., Zhang, W., Seitkhan, A., Neophytou, M., Faber, H., et al. (2020). 17.1% Efficient Single-Junction Organic Solar Cells Enabled by n-Type Doping of the Bulk-Heterojunction. Adv. Sci. *7*, 1903419. https://doi.org/10.1002/advs.201903419.

8. Fan, B., Zhang, D., Li, M., Zhong, W., Zeng, Z., Ying, L., Huang, F., and Cao, Y. (2019). Achieving over 16% efficiency for single-junction organic solar cells. Sci. China Chem. *62*, 746–752. https://doi.org/10.1007/s11426-019-9457-5.

9. Cui, Y., Yao, H., Zhang, J., Zhang, T., Wang, Y., Hong, L., Xian, K., Xu, B., Zhang, S., Peng, J., et al. (2019). Over 16% efficiency organic photovoltaic cells enabled by a chlorinated acceptor with increased open-circuit voltages. Nat. Commun. *10*, 2515. https://doi.org/10.1038/s41467-019-10351-5.

10. Cui, Y., Yao, H., Hong, L., Zhang, T., Tang, Y., Lin, B., Xian, K., Gao, B., An, C., Bi, P., et al. (2020). Organic photovoltaic cell with 17% efficiency and superior processability. Natl. Sci. Rev. *7*, 1239–1246. https://doi.org/10.1093/nsr/nwz200.

11. Chen, H., Zhang, R., Chen, X., Zeng, G., Kobera, L., Abbrent, S., Zhang, B., Chen, W., Xu, G., Oh, J., et al. (2021). A guest-assisted molecular-organization approach for >17% efficiency organic solar cells using environmentally friendly solvents. Nat. Energy *6*, 1045–1053. https://doi.org/10.1038/s41560-021-00923-5.

12. Cho, Y., Kumari, T., Jeong, S., Lee, S.M., Jeong, M., Lee, B., Oh, J., Zhang, Y., Huang, B., Chen, L., and Yang, C. (2020). Guest-oriented non-fullerene acceptors for ternary organic solar cells with over 16.0% and 22.7% efficiencies under one-sun and indoor light. Nano Energy *75*, 104896. https://doi.org/10.1016/j.nanoen.2020.104896.

13. Kan, Y., Sun, Y., Ren, Y., Xu, Y., Jiang, X., Shen, H., Geng, L., Li, J., Cai, P., Xu, H., et al. (2024). Amino-Functionalized Graphdiyne Derivative as a Cathode Interface Layer with High Thickness Tolerance for Highly Efficient Organic Solar Cells. Adv. Mater. *36*, 2312635. https://doi.org/10.1002/adma.202312635.

14. Ma, R., Zhou, K., Sun, Y., Liu, T., Kan, Y., Xiao, Y., Dela Peña, T.A., Li, Y., Zou, X., Xing, Z., et al. (2022). Achieving high efficiency and well-kept ductility in ternary all-polymer organic photovoltaic blends thanks to two well miscible donors. Matter *5*, 725–734. https://doi.org/10.1016/j.matt.2021.12.002.

15. Brabec, C.J., Distler, A., Du, X., Egelhaaf, H.-J., Hauch, J., Heumueller, T., and Li, N. (2020). Material Strategies to Accelerate OPV Technology Toward a GW Technology. Adv. Energy Mater. *10*, 2001864. https://doi.org/10.1002/aenm.202001864.

16. He, Y., Li, N., Heumüller, T., Wortmann, J., Hanisch, B., Aubele, A., Lucas, S., Feng, G., Jiang, X., Li, W., et al. (2022). Industrial viability of single-component organic solar cells. Joule *6*, 1160–1171. https://doi.org/10.1016/j.joule.2022.05.008.

17. Speller, E.M., Clarke, A.J., Aristidou, N., Wyatt, M.F., Francàs, L., Fish, G., Cha, H., Lee, H.K.H., Luke, J., Wadsworth, A., et al. (2019). Toward Improved Environmental Stability of Polymer:Fullerene and Polymer:Nonfullerene Organic Solar Cells: A Common Energetic Origin of Light- and Oxygen-Induced Degradation. ACS Energy Lett. *4*, 846–852. https://doi.org/10.1021/acsenergylett.9b00109.

18. Jørgensen, M., Norrman, K., Gevorgyan, S.A., Tromholt, T., Andreasen, B., and Krebs, F.C. (2012). Stability of Polymer Solar Cells. Adv. Mater. *24*, 580–612. https://doi.org/10.1002/adma.201104187.

19. Li, N., Perea, J.D., Kassar, T., Richter, M., Heumueller, T., Matt, G.J., Hou, Y., Güldal, N.S., Chen, H., Chen, S., et al. (2017). Abnormal strong burn-in degradation of highly efficient polymer solar cells caused by spinodal donor-acceptor demixing. Nat. Commun. *8*, 14541. https://doi.org/10.1038/ncomms14541.

20. Lorch, C., Frank, H., Banerjee, R., Hinderhofer, A., Gerlach, A., Li Destri, G., and Schreiber, F. (2015). Controlling length-scales of the phase separation to optimize organic semiconductor blends. Appl. Phys. Lett. *107*. https://doi.org/10.1063/1.4935545.

21. Zhu, L., Zhang, M., Zhong, W., Leng, S., Zhou, G., Zou, Y., Su, X., Ding, H., Gu, P., Liu, F., and Zhang, Y. (2021). Progress and prospects of the morphology of non-fullerene acceptor based high-efficiency organic solar cells. Energy Environ. Sci. *14*, 4341–4357. https://doi.org/10.1039/D1EE01220G.

22. Zhou, Z., Xu, S., Song, J., Jin, Y., Yue, Q., Qian, Y., Liu, F., Zhang, F., and Zhu, X. (2018). High-efficiency small-molecule ternary solar cells with a hierarchical morphology enabled by synergizing fullerene and non-fullerene acceptors. Nat. Energy *3*, 952–959. https://doi.org/10.1038/s41560-018-0234-9.

23. Halls, J.J.M., Pichler, K., Friend, R.H., Moratti, S.C., and Holmes, A.B. (1996). Exciton diffusion and dissociation in a poly(p-phenylenevinylene)/C60 heterojunction photovoltaic cell. Appl. Phys. Lett. *68*, 3120–3122. https://doi.org/10.1063/1.115797.

24. Heeger, A.J. (2014). 25th Anniversary Article: Bulk Heterojunction Solar Cells: Understanding the Mechanism of Operation. Adv. Mater. *26*, 10–27. https://doi.org/10.1002/adma.201304373.

25. Yu, G., and Heeger, A.J. (1995). Charge separation and photovoltaic conversion in polymer composites with internal donor/acceptor heterojunctions. J. Appl. Phys. *78*, 4510–4515. https://doi.org/10.1063/1.359792.

26. Kumari, T., Moon, M., Kang, S.-H., and Yang, C. (2016). Improved efficiency of DTGe(FBTTh2)2-based solar cells by using macromolecular additives: How macromolecular additives versus small additives influence nanoscale morphology and photovoltaic performance. Nano Energy *24*, 56–62. https://doi.org/10.1016/j.nanoen.2016.03.026.

27. Kumari, T., Lee, S.M., Kang, S.-H., Chen, S., and Yang, C. (2017). Ternary solar cells with a mixed face-on and edge-on orientation enable an unprecedented efficiency of 12.1%. Energy Environ. Sci. *10*, 258–265. https://doi.org/10.1039/C6EE02851A.

28. Zhao, W., Li, S., Yao, H., Zhang, S., Zhang, Y., Yang, B., and Hou, J. (2017). Molecular Optimization Enables over 13% Efficiency in Organic Solar Cells. J. Am. Chem. Soc. *139*, 7148–7151. https://doi.org/10.1021/jacs.7b02677.

29. Bertho, S., Janssen, G., Cleij, T.J., Conings, B., Moons, W., Gadisa, A., D'Haen, J., Goovaerts, E., Lutsen, L., Manca, J., and Vanderzande, D. (2008). Effect of temperature on the morphological and photovoltaic stability of bulk heterojunction polymer:fullerene solar cells. Sol. Energy Mater. Sol. Cells *92*, 753–760. https://doi.org/10.1016/j.solmat.2008.01.006.

30. Schaffer, C.J., Palumbiny, C.M., Niedermeier, M.A., Jendrzejewski, C., Santoro, G., Roth, S.V., and Müller-Buschbaum, P. (2013). A Direct Evidence of Morphological Degradation on a Nanometer Scale in Polymer Solar Cells. Adv. Mater. *25*, 6760–6764. https://doi.org/10.1002/adma.201302854.

31. Ye, L., Collins, B.A., Jiao, X., Zhao, J., Yan, H., and Ade, H. (2018). Miscibility–Function Relations in Organic Solar Cells: Significance of Optimal Miscibility in Relation to Percolation. Adv. Energy Mater. *8*, 1703058. https://doi.org/10.1002/aenm.201703058.

32. Kozub, D.R., Vakhshouri, K., Orme, L.M., Wang, C., Hexemer, A., and Gomez, E.D. (2011). Polymer Crystallization of Partially Miscible Polythiophene/Fullerene Mixtures Controls Morphology. Macromolecules *44*, 5722–5726. https://doi.org/10.1021/ma200855r.

33. Wang, R., Lüer, L., Langner, S., Heumueller, T., Forberich, K., Zhang, H., Hauch, J., Li, N., and Brabec, C.J. (2021). Understanding the Microstructure Formation of Polymer Films by Spontaneous Solution Spreading Coating with a High-Throughput Engineering Platform. ChemSusChem *14*, 3590–3598. https://doi.org/10.1002/cssc.202100927.

34. Gasparini, N., Jiao, X., Heumueller, T., Baran, D., Matt, G.J., Fladischer, S., Spiecker, E., Ade, H., Brabec, C.J., and Ameri, T. (2016). Designing ternary blend bulk heterojunction solar cells with reduced carrier recombination and a fill factor of 77%. Nat. Energy *1*, 16118. https://doi.org/10.1038/nenergy.2016.118.

35. Jiang, K., Zhang, J., Peng, Z., Lin, F., Wu, S., Li, Z., Chen, Y., Yan, H., Ade, H., Zhu, Z., and Jen, A.K.Y. (2021). Pseudo-bilayer architecture enables high-performance organic solar cells with enhanced exciton diffusion length. Nat. Commun. *12*, 468. https://doi.org/10.1038/s41467-020-20791-z.

36. Kumari, T., Jung, S., Cho, Y., Kim, H.-P., Lee, J.W., Oh, J., Lee, J., Lee, S.M., Jeong, M., Baik, J.M., et al. (2020). A built-in electric field induced by ferroelectrics increases halogen-free organic solar cell efficiency in various device types. Nano Energy *68*, 104327. https://doi.org/10.1016/j.nanoen.2019.104327.

37. Meng, L., Zhang, Y., Wan, X., Li, C., Zhang, X., Wang, Y., Ke, X., Xiao, Z., Ding, L., Xia, R., et al. (2018). Organic and solution-processed tandem solar cells with 17.3% efficiency. Science *361*, 1094–1098. https://doi.org/10.1126/science.aat2612.

38. Yu, R., Wu, G., Cui, Y., Wei, X., Hong, L., Zhang, T., Zou, C., Hu, S., Hou, J., and Tan, Z. (2021). Multi-Functional Solid Additive Induced

Favorable Vertical Phase Separation and Ordered Molecular Packing for Highly Efficient Layer-by-Layer Organic Solar Cells. Small *17*, 2103497. https://doi.org/10.1002/smll.202103497.

39. Ghasemi, M., Balar, N., Peng, Z., Hu, H., Qin, Y., Kim, T., Rech, J.J., Bidwell, M., Mask, W., McCulloch, I., et al. (2021). A molecular interaction–diffusion framework for predicting organic solar cell stability. Nat. Mater. *20*, 525–532. https://doi.org/10.1038/s41563-020-00872-6.

40. Brabec, C.J., Gowrisanker, S., Halls, J.J.M., Laird, D., Jia, S., and Williams, S.P. (2010). Polymer–Fullerene Bulk-Heterojunction Solar Cells. Adv. Mater. *22*, 3839–3856. https://doi.org/10.1002/adma.200903697.

41. Li, N., Machui, F., Waller, D., Koppe, M., and Brabec, C.J. (2011). Determination of phase diagrams of binary and ternary organic semiconductor blends for organic photovoltaic devices. Sol. Energy Mater. Sol. Cells *95*, 3465–3471. https://doi.org/10.1016/j.solmat.2011.08.005.

42. Mateker, W.R., and McGehee, M.D. (2017). Progress in Understanding Degradation Mechanisms and Improving Stability in Organic Photovoltaics. Adv. Mater. *29*, 1603940. https://doi.org/10.1002/adma.201603940.

43. Hong, L., Yao, H., Cui, Y., Bi, P., Zhang, T., Cheng, Y., Zu, Y., Qin, J., Yu, R., Ge, Z., and Hou, J. (2021). 18.5% Efficiency Organic Solar Cells with a Hybrid Planar/Bulk Heterojunction. Adv. Mater. *33*, 2103091. https://doi.org/10.1002/adma.202103091.

44. Wu, Q., Wang, W., Wu, Y., Chen, Z., Guo, J., Sun, R., Guo, J., Yang, Y.M., and Min, J. (2021). High-Performance All-Polymer Solar Cells with a Pseudo-Bilayer Configuration Enabled by a Stepwise Optimization Strategy. Adv. Funct. Mater. *31*, 2010411. https://doi.org/10.1002/adfm.202010411.

45. Zhou, M., Liao, C., Duan, Y., Xu, X., Yu, L., Li, R., and Peng, Q. (2023). 19.10% Efficiency and 80.5% Fill Factor Layer-by-Layer Organic Solar Cells Realized by 4-Bis(2-Thienyl)Pyrrole-2,5-Dione Based Polymer Additives for Inducing Vertical Segregation Morphology. Adv. Mater. *35*, 2208279. https://doi.org/10.1002/adma.202208279.

46. Lai, X., Lai, H., Du, M., Chen, H., Qiu, D., Zhu, Y., Pu, M., Zhu, Y., Zhou, E., and He, F. (2022). Bilayer Quasiplanar Heterojunction Organic Solar Cells with a Co-Acceptor: A Synergistic Approach for Stability and Efficiency. Chem. Mater. *34*, 7886–7896. https://doi.org/10.1021/acs.chemmater.2c01604.

47. Sun, Y., Nian, L., Kan, Y., Ren, Y., Chen, Z., Zhu, L., Zhang, M., Yin, H., Xu, H., Li, J., et al. (2022). Rational control of sequential morphology evolution and vertical distribution toward 17.18% efficiency all-small-molecule organic solar cells. Joule *6*, 2835–2848. https://doi.org/10.1016/j.joule.2022.10.005.

48. Cai, Y., Li, Q., Lu, G., Ryu, H.S., Li, Y., Jin, H., Chen, Z., Tang, Z., Lu, G., Hao, X., et al. (2022). Vertically optimized phase separation with improved exciton diffusion enables efficient organic solar cells with thick active layers. Nat. Commun. *13*, 2369. https://doi.org/10.1038/s41467-022-29803-6.

49. Firdaus, Y., Le Corre, V.M., Karuthedath, S., Liu, W., Markina, A., Huang, W., Chattopadhyay, S., Nahid, M.M., Nugraha, M.I., Lin, Y., et al. (2020). Long-range exciton diffusion in molecular non-fullerene acceptors. Nat. Commun. *11*, 5220. https://doi.org/10.1038/s41467-020-19029-9.

50. Hume, P.A., Jiao, W., and Hodgkiss, J.M. (2021). Long-range exciton diffusion in a non-fullerene acceptor: approaching the incoherent limit. J. Mater. Chem. C *9*, 1419–1428. https://doi.org/10.1039/D0TC05697A.

51. Xu, W., Ma, X., Son, J.H., Jeong, S.Y., Niu, L., Xu, C., Zhang, S., Zhou, Z., Gao, J., Woo, H.Y., et al. (2022). Smart Ternary Strategy in Promoting the Performance of Polymer Solar Cells Based on Bulk-Heterojunction or Layer-By-Layer Structure. Small *18*, 2104215. https://doi.org/10.1002/smll.202104215.

52. Zheng, Y., Sun, R., Zhang, M., Chen, Z., Peng, Z., Wu, Q., Yuan, X., Yu, Y., Wang, T., Wu, Y., et al. (2021). Baseplate Temperature-Dependent Vertical Composition Gradient in Pseudo-Bilayer Films for Printing Non-Fullerene Organic Solar Cells. Adv. Energy Mater. *11*, 2102135. https://doi.org/10.1002/aenm.202102135.

53. Kumari, T., Oh, J., Lee, S.M., Jeong, M., Lee, J., Lee, B., Kang, S.-H., and Yang, C. (2021). Over 13.8% efficiency of organic solar cells fabricated by air-processable spontaneously spreading process through water temperature control. Nano Energy *85*, 105982. https://doi.org/10.1016/j.nanoen.2021.105982.

54. Khenkin, M.V., Katz, E.A., Abate, A., Bardizza, G., Berry, J.J., Brabec, C., Brunetti, F., Bulović, V., Burlingame, Q., Di Carlo, A., et al. (2020). Consensus statement for stability assessment and reporting for perovskite photovoltaics based on ISOS procedures. Nat. Energy *5*, 35–49. https://doi.org/10.1038/s41560-019-0529-5.

55. Kumari, T., Ahmadpour, M., Morin, P.-O., Ahmad, M., Atajanov, R., Rindom, C., Oh, J., Yakoob, M.A., Bergeron, J.-S., Grenier, F., et al. (2023). Role of Nonfullerene Acceptor Impurities and Purification on the Efficiency and Stability of Organic Photovoltaics. Sol. RRL *7*, 2300047. https://doi.org/10.1002/solr.202300047.

56. Lee, S.M., Kumari, T., Lee, B., Cho, Y., Lee, J., Oh, J., Jeong, M., Jung, S., and Yang, C. (2020). Horizontal-Vertical-and Cross-Conjugated Small Molecules: Conjugated Pathway-Performance Correlations along Operation Mechanisms in Ternary Non-Fullerene Organic Solar Cells. Small *16*, 1905309. https://doi.org/10.1002/smll.201905309.

57. Hu, H., Deng, W., Qin, M., Yin, H., Lau, T.-K., Fong, P.W., Ren, Z., Liang, Q., Cui, L., Wu, H., et al. (2019). Charge carrier transport and nanomorphology control for efficient non-fullerene organic solar cells. Mater. Today Energy *12*, 398–407. https://doi.org/10.1016/j.mtener.2019.04.005.

58. Li, S., Li, C.-Z., Shi, M., and Chen, H. (2020). New Phase for Organic Solar Cell Research: Emergence of Y-Series Electron Acceptors and Their Perspectives. ACS Energy Lett. *5*, 1554–1567. https://doi.org/10.1021/acsenergylett.0c00537.

59. Xiang, C., Zhao, Q., Liu, W., Cao, J., Zou, Y., and Zhou, H. (2022). Theoretical exploration of molecular packing and the charge transfer mechanism of organic solar cells based on PM6:Y6. J. Mater. Chem. A *10*, 25611–25619. https://doi.org/10.1039/D2TA07420F.

60. Kroh, D., Athanasopoulos, S., Nádaždy, V., Kahle, F.-J., Bässler, H., and Köhler, A. (2023). An Impedance Study of the Density of States Distribution in Blends of PM6:Y6 in Relation to Barrierless Dissociation of CT States. Adv. Func. Mater. 2302520. https://doi.org/10.1002/adfm.202302520.

61. Zhang, G., Chen, X.-K., Xiao, J., Chow, P.C.Y., Ren, M., Kupgan, G., Jiao, X., Chan, C.C.S., Du, X., Xia, R., et al. (2020). Delocalization of exciton and electron wavefunction in non-fullerene acceptor molecules enables efficient organic solar cells. Nat. Commun. *11*, 3943. https://doi.org/10.1038/s41467-020-17867-1.

62. Würfel, U., Cuevas, A., and Würfel, P. (2015). Charge Carrier Separation in Solar Cells. IEEE J. Photovolt. *5*, 461–469. https://doi.org/10.1109/JPHOTOV.2014.2363550.

63. Vaynzof, Y., Kabra, D., Zhao, L., Ho, P.K.H., Wee, A.T.-S., and Friend, R.H. (2010). Improved photoinduced charge carriers separation in organic-inorganic hybrid photovoltaic devices. Appl. Phys. Lett. *97*, 033309. https://doi.org/10.1063/1.3464973.

64. Schilinsky, P., Waldauf, C., and Brabec, C.J. (2002). Recombination and loss analysis in polythiophene based bulk heterojunction photodetectors. Appl. Phys. Lett. *81*, 3885–3887. https://doi.org/10.1063/1.1521244.

65. Riedel, I., Parisi, J., Dyakonov, V., Lutsen, L., Vanderzande, D., and Hummelen, J.C. (2004). Effect of Temperature and Illumination on the Electrical Characteristics of Polymer–Fullerene Bulk-Heterojunction Solar Cells. Adv. Funct. Mater. *14*, 38–44. https://doi.org/10.1002/adfm.200304399.

66. Zhu, X., Wang, K., He, J., Zhang, L., Yu, H., He, D., and Hu, B. (2019). Exploring Deep and Shallow Trap States in a Non-Fullerene Acceptor ITIC-Based Organic Bulk Heterojunction Photovoltaic System. J. Phys. Chem. C *123*, 20691–20697. https://doi.org/10.1021/acs.jpcc.9b03515.

67. Wu, J., Lee, J., Chin, Y.-C., Yao, H., Cha, H., Luke, J., Hou, J., Kim, J.-S., and Durrant, J.R. (2020). Exceptionally low charge trapping enables highly efficient organic bulk heterojunction solar cells. Energy Environ. Sci. *13*, 2422–2430. https://doi.org/10.1039/D0EE01338B.

68. Sandberg, O.J., Tvingstedt, K., Meredith, P., and Armin, A. (2019). Theoretical Perspective on Transient Photovoltage and Charge Extraction Techniques. J. Phys. Chem. C *123*, 14261–14271. https://doi.org/10.1021/acs.jpcc.9b03133.

69. Meng, L., Sun, C., Wang, R., Huang, W., Zhao, Z., Sun, P., Huang, T., Xue, J., Lee, J.-W., Zhu, C., et al. (2018). Tailored Phase Conversion under Conjugated Polymer Enables Thermally Stable Perovskite Solar Cells with Efficiency Exceeding 21. J. Am. Chem. Soc. *140*, 17255–17262. https://doi.org/10.1021/jacs.8b10520.

70. Barnes, P.R.F., Miettunen, K., Li, X., Anderson, A.Y., Bessho, T., Gratzel, M., and O'Regan, B.C. (2013). Interpretation of Optoelectronic Transient and Charge Extraction Measurements in Dye-Sensitized Solar Cells. Adv. Mater. *25*, 1881–1922. https://doi.org/10.1002/adma.201201372.

71. Kumari, T., Lee, S.M., and Yang, C. (2018). Cubic-Like Bimolecular Crystal Evolution and over 12% Efficiency in Halogen-Free Ternary Solar Cells. Adv. Funct. Mater. *28*, 1707278. https://doi.org/10.1002/adfm.201707278.

72. Zhang, Y., He, Y., Zeng, L., Lüer, L., Deng, W., Chen, Y., Zhou, J., Wang, Z., Brabec, C.J., Wu, H., et al. (2023). Unraveling the Role of Non-Fullerene Acceptor with High Dielectric Constant in Organic Solar Cells. Small *19*, 2302314. https://doi.org/10.1002/smll.202302314.

73. Leever, B.J., Bailey, C.A., Marks, T.J., Hersam, M.C., and Durstock, M.F. (2012). In Situ Characterization of Lifetime and Morphology in Operating Bulk Heterojunction Organic Photovoltaic Devices by Impedance Spectroscopy. Adv. Energy Mater. *2*, 120–128. https://doi.org/10.1002/aenm.201100357.

74. Kumari, T., Lee, S.M., Lee, K.C., Cho, Y., and Yang, C. (2018). Harmonious Compatibility Dominates Influence of Side-Chain Engineering on Morphology and Performance of Ternary Solar Cells. Adv. Energy Mater. *8*, 1800616. https://doi.org/10.1002/aenm.201800616.

75. Bhandari, S., Roy, A., Ghosh, A., Mallick, T.K., and Sundaram, S. (2020). Performance of WO3-Incorporated Carbon Electrodes for Ambient Mesoscopic Perovskite Solar Cells. ACS Omega *5*, 422–429. https://doi.org/10.1021/acsomega.9b02934.

76. Cui, Y., Yao, H., Hong, L., Zhang, T., Xu, Y., Xian, K., Gao, B., Qin, J., Zhang, J., Wei, Z., and Hou, J. (2019). Achieving Over 15% Efficiency in Organic Photovoltaic Cells via Copolymer Design. Adv. Mater. *31*, 1808356. https://doi.org/10.1002/adma.201808356.

77. Ciammaruchi, L., Zapata-Arteaga, O., Gutiérrez-Fernández, E., Martin, J., and Campoy-Quiles, M. (2020). Structure dependent photostability of ITIC and ITIC-4F. Mater. Adv. *1*, 2846–2861. https://doi.org/10.1039/D0MA00458H.

78. Doumon, N.Y., Houard, F.V., Dong, J., Yao, H., Portale, G., Hou, J., and Koster, L.J.A. (2019). Energy level modulation of ITIC derivatives: Effects on the photodegradation of conventional and inverted organic solar cells. Org. Electron. *69*, 255–262. https://doi.org/10.1016/j.orgel.2019.03.037.

79. Park, S., Kim, T., Yoon, S., Koh, C.W., Woo, H.Y., and Son, H.J. (2020). Progress in Materials, Solution Processes, and Long-Term Stability for Large-Area Organic Photovoltaics. Adv. Mater. *32*, 2002217. https://doi.org/10.1002/adma.202002217.

80. An, K., Zhong, W., Peng, F., Deng, W., Shang, Y., Quan, H., Qiu, H., Wang, C., Liu, F., Wu, H., et al. (2023). Mastering morphology of non-fullerene acceptors towards long-term stable organic solar cells. Nat. Commun. *14*, 2688. https://doi.org/10.1038/s41467-023-38306-x.

81. Liu, T., Burlingame, Q.C., Ivancevic, M.R., Liu, X., Hu, J., Rand, B.P., and Loo, Y.-L. (2023). Photochemical Decomposition of Y-Series Non-Fullerene Acceptors Is Responsible for Degradation of High-Efficiency Organic Solar Cells. Adv. Energy Mater. *13*, 2300046. https://doi.org/10.1002/aenm.202300046.

82. Jia, Z., Chen, Z., Chen, X., Yao, J., Yan, B., Sheng, R., Zhu, H., and Yang, Y.M. (2021). 19.34 cm^2 large-area quaternary organic photovoltaic module with 12.36% certified efficiency. Photonics Res. *9*, 324–330. https://doi.org/10.1364/PRJ.416229.

83. Ma, B., Lin, H., Li, M., Yu, X., Li, X., Du, X., Yang, G., Zheng, C., and Tao, S. (2022). Hydrogen-bond-induced cathode engineering interface achieving high-efficiency organic solar cells. J. Mater. Chem. C *10*, 6358–6364. https://doi.org/10.1039/D1TC05129F.

84. Yang, X., Li, B., Zhang, X., Li, S., Zhang, Q., Yuan, L., Ko, D.-H., Ma, W., and Yuan, J. (2023). Intrinsic Role of Volatile Solid Additive in High-Efficiency PM6:Y6 Series Nonfullerene Solar Cells. Adv. Mater. *35*, 2301604. https://doi.org/10.1002/adma.202301604.

85. van der Pol, T.P.A., van Gorkom, B.T., van Geel, W.F.M., Littmann, J., Wienk, M.M., and Janssen, R.A.J. (2023). Origin, Nature, and Location of Defects in PM6:Y6 Organic Solar Cells. Adv. Energy Mater. *13*, 2300003. https://doi.org/10.1002/aenm.202300003.

86. Schauer, F. (2020). Electronic structure spectroscopy of organic semiconductors by energy resolved-electrochemical impedance spectroscopy (ER-EIS). J. Appl. Phys. *128*. https://doi.org/10.1063/5.0022289.

87. Bässler, H., Kroh, D., Schauer, F., Nádaždy, V., and Köhler, A. (2021). Mapping the Density of States Distribution of Organic Semiconductors by Employing Energy Resolved–Electrochemical Impedance Spectroscopy. Adv. Func. Mater. *31*, 2007738. https://doi.org/10.1002/adfm.202007738.

88. Clarke, A.J., Luke, J., Meitzner, R., Wu, J., Wang, Y., Lee, H.K., Speller, E.M., Bristow, H., Cha, H., Newman, M.J., et al. (2021). Non-fullerene acceptor photostability and its impact on organic solar cell lifetime*2*, pp. 100498. https://doi.org/10.1016/j.xcrp.2021.100498.

89. Wang, Z., Nian, Y., Jiang, H., Pan, F., Hu, Z., Zhang, L., Cao, Y., and Chen, J. (2019). High Voc ternary nonfullerene polymer solar cells with improved efficiency and good thermal stability. Org. Electron. *69*, 174–180. https://doi.org/10.1016/j.orgel.2019.03.030.

90. Liao, C.-Y., Chen, Y., Lee, C.-C., Wang, G., Teng, N.-W., Lee, C.-H., Li, W.-L., Chen, Y.-K., Li, C.-H., Ho, H.-L., et al. (2020). Processing Strategies for an Organic Photovoltaic Module with over 10% Efficiency. Joule *4*, 189–206. https://doi.org/10.1016/j.joule.2019.11.006.